PCCP

PAPER

View Article Online
View Journal | View Issue

Cite this: *Phys. Chem. Chem. Phys.*, 2017, **19**, 26310

Modeling the impedance spectra of mixed conducting thin films with exposed and embedded current collectors†

Jiapeng Liu[a] and Francesco Ciucci *[ab]

Received 1st June 2017,
Accepted 12th September 2017

DOI: 10.1039/c7cp03703a

rsc.li/pccp

In this article, we develop a new finite-element-based model for the simulation of the electrochemical impedance spectroscopy (EIS) response of mixed ionic electronic conducting (MIEC) thin films. We first validated the model against experimental data for Sm-doped CeO_2 (SDC) symmetrical films deposited on an yittria-stabilized ZrO_2 (YSZ) substrate, a pure ionic conductor. We first studied the configuration where the patterned electrodes are placed on top of the MIEC ("exposed" configuration). Our model is capable of correctly reproducing the EIS response and the total capacitance, together with their dependence on the oxygen partial pressure. Furthermore, we were able to show, in agreement with experiments, that the area specific resistance (R_p) is relatively insensitive to the density of triple phase boundaries. As a second step, we studied the configuration where the metal current collector is directly deposited on the ionic conductor and is, therefore, "embedded" into the MIEC. We were again able to reproduce the experimental EIS response. We also discovered that at sufficiently high frequencies, the EIS deviates from a traditional RC-type response, leading to features attributable to the coupling ionic and electronic transport. This coupling ultimately adds to the area specific resistance. The latter, however, can be minimized if the film is sufficiently thick or if the current collector configuration is chosen judiciously.

1 Introduction

Sustainable energy technologies with high efficiency and fuel flexibility are needed in order to curb global warming and limit environmental pollution.[1] Solid oxide fuel cells (SOFCs) will likely play an important role in this area because, with heat recuperation, their efficiency can exceed 60%.[2] Furthermore, SOFCs can be operated on a number of fuels, including H_2, natural gas, propane, *etc.*[2] However, one of the bottlenecks of the SOFC technology is the poor performance of the electrodes.[3–5] In traditional electrodes, such as Ni/YSZ cermets,[6] the electrochemical reactions take place at the three phase boundary (3PB), the region where the three chemically active phases (gaseous, ionic conductor, and electronic conductor), meet.[7] This geometrical limitation can be overcome by mixed ionic–electronic conductors (MIEC), which are capable of extending the active reaction zone beyond the 3PB to the entire two phase boundary (2PB) (*i.e.* the gas|electrode interface), thanks to their intrinsic electronic conductivity. MIEC materials have found numerous applications in SOFCs both as cathodes (*e.g.* (La,Sr)$CoO_{3-\delta}$,[8] $Ba_{0.5}Sr_{0.5}Co_{0.8}Fe_{0.2}O_{3-\delta}$ (BSCF),[9] $La_{0.8}Sr_{0.2}MnO_{3-\delta}$ (LSM)[10] and $Ba_{0.95}La_{0.05}FeO_{3-\delta}$ (BLF)[11]), and as anodes, (*e.g.* $Sm_xCe_{1-x}O_{2-\delta}$ (SDC),[12–17] $Ce_xGd_{1-x}O_{2-\delta}$ (GDC),[18] $La_{0.6}Sr_{0.4}Co_{0.2}Fe_{0.8}O_{3-\delta}$ (LSCF),[19] $La_xSr_{1-3x/2}TiO_3$ (LST),[20] and $La_{0.43}Ca_{0.37}Ni_{0.06}Ti_{0.94}O_3$ (LCNT)[21]). However, the most widely used electrode materials at the anode of industrial grade SOFCs are still not MIECs.

In order to improve and eventually use MIECs in real SOFCs, it is critical to understand their electrocatalytic properties. Unfortunately, experimental studies typically utilize porous electrodes,[6,22–25] which have complicated and non-controllable geometries. In turn, this complexity makes the identification of the reaction pathways particularly difficult.[26] In contrast, well characterized geometries, such as those of dense thin films, result in a better identification of the electrocatalytic mechanism.[17,27–32] Mizusaki and co-workers[33] pioneered this approach by placing a regular and well-characterized pattern of current collecting metal strips on top of MIEC films. However, pattern current collectors have the adverse effect of reducing the surface available for chemical reactions. Furthermore, as shown in our earlier work, if the metal strips of the pattern are sufficiently large and widely spaced, they can significantly

[a] *Department of Mechanical and Aerospace Engineering, The Hong Kong University of Science and Technology, Hong Kong, China. E-mail: mefrank@ust.hk; Tel: +852 2358 7187*

[b] *Department of Chemical and Biomolecular Engineering, The Hong Kong University of Science and Technology, Hong Kong, China*

† Electronic supplementary information (ESI) available. See DOI: 10.1039/c7cp03703a

affect the electrochemical response.[34] In principle, one can overcome these challenges by embedding the entire current collector into the MIEC film. This configuration not only extends the active reaction zone to the entire exposed MIEC area[3,26,35] and, therefore, lowers the impedance, but it also enables the utilization of a number of *operando* characterization methods, including ambient pressure X-ray Photoelectron Spectroscopy.[15,36]

Electrochemical impedance spectroscopy (EIS) is one of the most widely used experimental techniques for the characterization of electroactive materials. In EIS, a small sinusoidal current/bias is applied to an electrochemical system in order to measure the resulting bias/current.[37,38] If this procedure is repeated over numerous frequencies, it leads to significant insight into the system under study, including the electrocatalytic mechanism. Equivalent circuit models (ECMs) are typically used to interpret the EIS response.[37,38] Even though it is relatively easy to fit EIS data using ECMs, ECMs are often chosen in an *ad hoc* fashion. For example, several equally plausible ECMs can be used to fit the data equally well, ultimately limiting the usefulness of EIS experiments.[39] To overcome these challenges, a number of research groups have developed numerical models based on fundamental physical and chemical principles.[26,34,40–54] In our own work, starting directly from the Poisson–Nernst–Planck equations and simple kinetics, we have established models capable of computing the EIS of both MIEC bulk samples and thin films.[34,40,41]

In this article, we computationally study the EIS response of MIEC thin film in two different configurations:

(i) A traditional patterned electrode with the metal current collectors placed on top of the MIEC (we denote this configuration as "exposed", see Fig. 1(a));

(ii) An electrode setup where the metal current collectors are embedded into the electrode itself (we denote this configuration as "embedded", see Fig. 1(b)).

Both configurations are assumed to be periodic and symmetric. While the presented model is general and can be applied to the study of the EIS response of any MIEC, we will focus on SDC. This is because SDC has been extensively investigated and experimental results are readily available.[3,12,32] Additionally, SDC has a number of advantages over the most widely used anode materials (*i.e.* Ni/YSZ), including an increased resistance to coking and poisoning.[16,55] In this work, we first derived an updated physical model based on our earlier work.[34,40,41] We then compared the new model against experimental data in the exposed configuration. Lastly, we validated the model against embedded current collector configuration. Interestingly, we found that the EIS response of SDC is sensitive to the film thickness and current collector configuration.

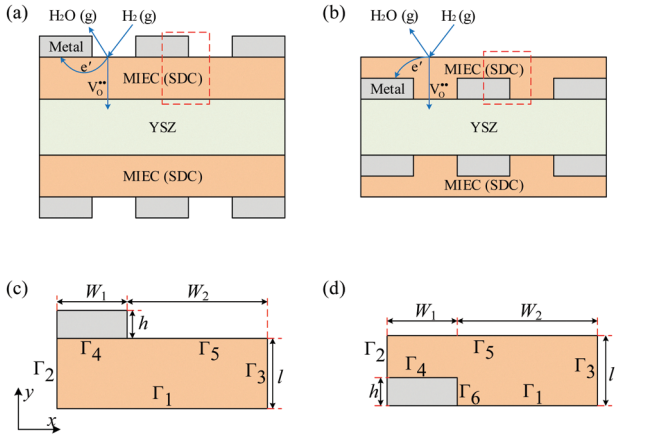

Fig. 1 Schematic of thin film samples. In the exposed configuration, panel (a), the current collector is deposited on the top surface. Instead, in the embedded configuration, panel (b), the current collector is inside the MIEC. Panels (c) and (d) label the boundaries of the numerical domain and provide their size.

2 Numerical model

We modeled the transport of polarons, e' and oxygen vacancies, $V_O^{\bullet\bullet}$ (the Kröger–Vink notation is used).[56] For convenience, the properties of e' and $V_O^{\bullet\bullet}$ are denoted with the subscripts "eon" and "ion", respectively. We consider that an immobile background dopant $\left(Sm_{Ce}'\right)$ is also present in SDC.[57] The subscript "B" is used for Sm_{Ce}'.

The MIEC is studied in reducing conditions, which result from exposing the material to an H_2-rich gas. The defect chemical model used is identical to the one employed in earlier publications.[34,40,41,57] The equilibrium concentration of polarons c_{eon}^0 increases upon reduction as follows[57]

$$c_{eon}^0 = \left(\frac{2K_r}{B}\right)^{1/2} \tilde{p}_{O_2}{}^{-1/4} \quad (1)$$

where the superscript "0" denotes that the concentration of polarons is that at equilibrium state, B is the concentration of the background dopant, $\tilde{p}_{O_2}$ is the normalized oxygen partial pressure ($\tilde{p}_{O_2} = p_{O_2}/1$ atm with p_{O_2} as the oxygen partial pressure), and the parameter K_r is the equilibrium constant of the reaction

$$O_O^{\times} \rightleftharpoons \frac{1}{2}O_2(\text{gas}) + V_O^{\bullet\bullet} + 2e' \quad (2)$$

where $O_O^{\times}$ is an oxygen site in SDC.

As shown in Fig. 1, the two configurations studied (exposed and embedded) differ in the placement of the current collectors. We simulated only a section of the entire material sample because of symmetry and periodicity, see Fig. 1(c) and (d). The geometry of the sample is defined by (i) the width, $2W_1$, of the metal strips; (ii) the distance, $2W_2$, between the strips; (iii) the film thickness, l; and (iv) the height, h, of the metal strips. The 2PB is assumed to be flat for both the configurations.

2.1 Poisson–Nernst–Planck equations for the transport of defects

In the bulk of the material, continuity of charge holds for all species. Following the assumption that there is no internal

generation or recombination of charge carriers,[58] the charge conservation law can be written as

$$z_i e\frac{\partial c_i}{\partial t} + \nabla \cdot \boldsymbol{j}_i = 0 \tag{3}$$

where e is the elementary electric charge, t is time, and c_i and z_i are the concentration and integer charge of species i (either e' or $V_O^{\bullet\bullet}$), respectively.

Additionally, $\boldsymbol{j}_i$, the current of species i, is defined as

$$\boldsymbol{j}_i = -\sigma_i \nabla \tilde{\mu}_i^* \tag{4}$$

where σ_i is its conductivity and $\tilde{\mu}_i^*$ is its reduced electrochemical potential. According to the Nernst–Einstein relation we can write

$$\sigma_i = (z_i e)^2 \frac{D_i c_i}{k_B T} \tag{5}$$

where D_i is the diffusivity, k_B is the Boltzmann constant, T is the temperature. The reduced electrochemical potential can be written as

$$\tilde{\mu}_i^* = \frac{\mu_i^0}{z_i e} + \frac{k_B T}{z_i e}\ln\frac{c_i}{c_i^0} + \phi \tag{6}$$

c_i^0 and μ_i^0 are the reference concentration and chemical potential, respectively, and, finally, ϕ is the electric potential.

Furthermore, Poisson's equation also holds

$$-\varepsilon\Delta\phi = e(2c_{ion} - c_{eon} - B) \tag{7}$$

where ε is the permittivity of the material.

Finally, the material properties for the simulations are identical to the ones used in our previous work[40,41] and for completeness are shown in Table 1.

2.2 Modeling the EIS response

During an EIS experiment, the electrochemical system under study is subjected to a small sinusoidal perturbation in either bias or current. Mathematically, this is a regular perturbation. Any physical quantity can be expressed as the sum of its steady state value plus the perturbation (denoted with δ),[50,59,60] *i.e.*,

$$\phi = \phi^0 + \delta\phi = \delta\phi \tag{8a}$$

$$c_i = c_i^0 + \delta c_i \tag{8b}$$

$$\tilde{\mu}_i^* = \tilde{\mu}_i^{*0} + \delta\tilde{\mu}_i^* \tag{8c}$$

Hereafter, we will drop ϕ^0 because we assumed that the electrochemical system is not subjected to a bias and that neutrality holds throughout. Furthermore, we can take that $\nabla(\cdot)^0 = 0$.

Table 1 Material properties at selected temperatures

Parameter	T = 600 °C	T = 650 °C
D_{ion}/m^2 s^{-1}	2.527×10^{-10}	3.927×10^{-10}
D_{eon}/m^2 s^{-1}	5.171×10^{-9}	6.462×10^{-9}
K_r	6.610×10^{-19}	1.340×10^{-17}

If we then (i) substitute (8) into (3) and (7); (ii) enforce charge neutrality; and (iii) discard terms above first order in δ, we can write

$$C_{chem}\partial_t(\delta\tilde{\mu}_{ion}^* - \delta\tilde{\mu}_{eon}^*) = \sigma_{ion}^0\Delta\delta\tilde{\mu}_{ion}^* \tag{9a}$$

$$C_{chem}\partial_t(\delta\tilde{\mu}_{eon}^* - \delta\tilde{\mu}_{ion}^*) = \sigma_{eon}^0\Delta\delta\tilde{\mu}_{eon}^* \tag{9b}$$

where the volume-specific chemical capacitance is defined as[50,57,60]

$$C_{chem} = \frac{e^2}{k_B T}\left(\frac{1}{z_{ion}^2 c_{ion}^0} + \frac{1}{z_{eon}^2 c_{eon}^0}\right)^{-1} \tag{10}$$

and the conductivities, σ_{ion}^0 and σ_{eon}^0, are obtained from (5), (1), and charge neutrality.

Further, we can recast (9) in dimensionless form by defining: (i) a dimensionless coordinate system $\tilde{\boldsymbol{x}} = \boldsymbol{x}/l_c$ with characteristic length l_c; (ii) dimensionless reduced electrochemical potentials $\bar{\mu}_i^* = \tilde{\mu}_i^*/U_T$ (with $U_T = k_B T/e$); and (iii) two time scales $\tau_{ion} = l_c^2 C_{chem}/\sigma_{ion}^0$, $\tau_{eon} = l_c^2 C_{chem}/\sigma_{eon}^0$. After Fourier transformation with respect to time,‡ we can rewrite (9) as

$$i\omega\tau_{ion}(\delta\hat{\mu}_{ion}^* - \delta\hat{\mu}_{eon}^*) = \Delta_{\tilde{\boldsymbol{x}}}\delta\hat{\mu}_{ion}^* \tag{11a}$$

$$i\omega\tau_{eon}(\delta\hat{\mu}_{eon}^* - \delta\hat{\mu}_{ion}^*) = \Delta_{\tilde{\boldsymbol{x}}}\delta\hat{\mu}_{eon}^* \tag{11b}$$

with $\delta\hat{\mu}_{ion}{}^* = \mathcal{F}(\delta\bar{\mu}_{ion}{}^*)$ and $\delta\hat{\mu}_{eon}{}^* = \mathcal{F}(\delta\bar{\mu}_{eon}{}^*)$, and $\omega = 2\pi f$ (f is the frequency).

2.3 Boundary conditions

2.3.1 Symmetrical boundary conditions. Due to periodicity at Γ_2 and Γ_3, the gradients of the reduced electrochemical potential along x direction are all 0, *i.e.*,

$$\partial_{\tilde{x}}\delta\hat{\mu}_{eon}^*|_{\Gamma_2} = \partial_{\tilde{x}}\delta\hat{\mu}_{eon}^*|_{\Gamma_3} = 0 \tag{12a}$$

$$\partial_{\tilde{x}}\delta\hat{\mu}_{ion}^*|_{\Gamma_2} = \partial_{\tilde{x}}\delta\hat{\mu}_{ion}^*|_{\Gamma_3} = 0 \tag{12b}$$

2.3.2 Ion and electron blocking boundaries. The presence of the YSZ, a pure ionic electrolyte, prevents the electrons from passing through the YSZ|MIEC interface. Similarly, the metal surface is ion-blocking. Therefore, the corresponding fluxes vanish:

$$\partial_{\tilde{y}}\delta\hat{\mu}_{eon}^*|_{\Gamma_1} = 0 \tag{13a}$$

$$\partial_{\tilde{y}}\delta\hat{\mu}_{ion}^*|_{\Gamma_4} = 0 \tag{13b}$$

Additionally, we assumed that the interface between the MIEC and the electrolyte is reversible and characterized by a constant electrochemical potential of oxygen vacancies.[34,40,41] This implies that there is no resistance to $V_O^{\bullet\bullet}$ migration across the YSZ|MIEC interface and that the electrochemical potential of $V_O^{\bullet\bullet}$ is identical on both sides of the interface. Furthermore, if we take that the flow of oxygen vacancies is unidirectional at that interface, we can write

$$\delta\hat{\mu}_{ion}^*|_{\Gamma_1} = 0 \tag{14}$$

‡ We choose the unitary Fourier transform: $\hat{g}(\omega) = \int_{-\infty}^{\infty} g(t)e^{-i\omega t}dt \cdot s$.

Due to linearity, the Fourier transform of the reduced dimensionless electrochemical potential of electrons at Γ_4 can be arbitrarily set to unity,[41] *i.e.*,

$$\delta\hat{\mu}_{\mathrm{eon}}{}^{\star}|_{\Gamma_4} = 1 \tag{15}$$

Lastly, for the embedded configuration, the electrochemical potential of e′ and $V_O^{\bullet\bullet}$ at Γ_6 are identical to that at Γ_4, *i.e.*, $\delta\hat{\mu}_{\mathrm{eon}}{}^{\star}|_{\Gamma_6} = 1$, $\partial_{\tilde{x}}\delta\hat{\mu}_{\mathrm{ion}}{}^{\star}|_{\Gamma_6} = 0$.

2.3.3 Chemical reaction at the MIEC|gas interface. We will assume a global reaction at the MIEC|gas interface (Γ_5):

where ions and electrons are injected into the system through the 2PB. Because only a small bias is applied to the sample, we can linearize the rate of (16). This leads to the following Chang–Jaffé boundary condition:[61]

$$\frac{1}{R_{\mathrm{surf}}} = \frac{\boldsymbol{j}_{\mathrm{ion}}\cdot\mathbf{n}|_{\Gamma_5}}{\delta\tilde{\mu}_{\mathrm{ion}}{}^{*} - \delta\tilde{\mu}_{\mathrm{eon}}{}^{*}} = k \tag{16}$$

where $\mathbf{n}$ is the unit normal vector pointing out of the MIEC, k is the surface reaction constant, and R_{surf} is the surface reaction resistance. We will take the rate constant to be[12,57]

$$k = k^0\tilde{p}_{O_2}^{-\beta} \tag{17}$$

where k^0 is a constant and β is a power coefficient drawn from either experiment or theory. In particular, β is either 0.25 for SDC-15 with exposed electrodes,[57] or 0.15 for SDC-20 with embedded current collectors.[3] The rate constant model above is used to simulate the material at oxygen partial pressures from 10^{-26} to 10^{-21} atm, the same range studied in the experiments.[3,57]

Following on our previous work,[34] the boundary conditions at Γ_5 can also include double layer effects and can be written as

$$\partial_{\bar{y}}\delta\hat{\mu}_{\mathrm{ion}}{}^{*} = -\frac{l_{\mathrm{c}}}{\sigma^0_{\mathrm{ion}}}\left(\frac{1}{R_{\mathrm{surf}}} + i\omega c^0_{\mathrm{ion}}C_0\right)(\delta\hat{\mu}_{\mathrm{ion}}{}^{*} - \delta\hat{\mu}_{\mathrm{eon}}{}^{*}) \tag{18a}$$

$$\partial_{\bar{y}}\delta\hat{\mu}_{\mathrm{eon}}{}^{*} = -\frac{l_{\mathrm{c}}}{\sigma^0_{\mathrm{eon}}}\left(\frac{1}{R_{\mathrm{surf}}} + \frac{i\omega c^0_{\mathrm{eon}}C_0}{4}\right)(\delta\hat{\mu}_{\mathrm{eon}}{}^{*} - \delta\hat{\mu}_{\mathrm{ion}}{}^{*}) \tag{18b}$$

and a detailed derivation is given in ESI,† Section S1.

2.4 Computational methods

The governing equations and the corresponding boundary conditions outlined above are solved with the finite element method using the package FreeFem++.[62] We discretized the computational domain on a triangular unstructured mesh and used quadratic P2 Lagrangian elements. For each computation, the mesh is optimized 14 times *a posteriori*. The first ten adaptations are performed against the 4-dimensional vector ($\mathrm{Re}[\nabla\delta\hat{\mu}_{\mathrm{ion}}{}^{\star}]$, $\mathrm{Re}[\nabla\delta\hat{\mu}_{\mathrm{eon}}{}^{\star}]$) and subsequently, the mesh is refined against η_e as defined in ESI,† Section S2.[41] The adaptation method guarantees that the mesh is fine enough to handle the severe gradients occurring at intersections between boundaries.[63] The physical parameters used in the numerical simulations are listed in Table 2.

3 Numerical results

3.1 Exposed electrode

3.1.1 Comparison against experimental data. In order to validate the developed model, we first compared the computed impedance response to the experimental data. The numerically computed impedance is the ratio of the Fourier-transformed electrochemical potential drop across the entire film divided by the Fourier-transformed current density collected at the metal surface,[40,41] *i.e.*,

$$Z = \frac{\hat{V}}{\hat{j}} \tag{19}$$

Specifically, the electrochemical potential drop is given by

$$\hat{V} = 2U_{\mathrm{T}}[\langle\delta\hat{\mu}_{\mathrm{eon}}{}^{\star}\rangle_{\Gamma_4} - \langle\delta\hat{\mu}_{\mathrm{ion}}{}^{\star}\rangle_{\Gamma_1}] = 2U_{\mathrm{T}} \tag{20}$$

where the factor 2 is included because we consider a symmetrical configuration and the second equality is obtained from (14) and (15). The current density is given by

$$\hat{j} = \frac{\sigma^0_{\mathrm{eon}}U_{\mathrm{T}}\int_{\Gamma_5}\mathbf{n}\cdot\nabla_{\tilde{x}}\delta\hat{\mu}_{\mathrm{eon}}{}^{*}\mathrm{d}\tilde{x}}{W_1 + W_2} \tag{21}$$

whose normalization area encompasses the whole extension of the film.

In order to separate the contributions of various resistances in the MIEC system, a 0-frequency ECM is schematically shown in Fig. 2. We particularly focus on $Z(f = 0)$ because, for this model, it is identical to twice the polarization resistance R_{p}. It is critical to note that R_{p} is one of the most important parameters

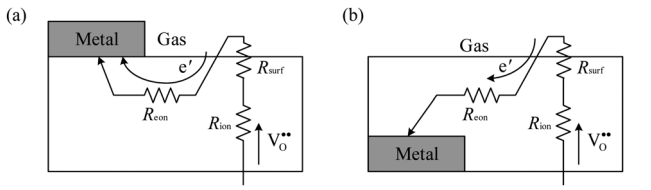

Fig. 2 Schematic of the currents and equivalent circuit model in the thin film in the exposed, (a), and embedded, (b), configurations, when $f = 0$.

Table 2 Values and range for the parameters of the EIS model

Parameter	Definition	Value
W_1	Width of the metal current collector	1–75 μm
W_2	Spacing distance between two current collectors	1–75 μm
l	The thickness of the thin film	195–800 nm
h	The height of the metal strips	150 nm
l_{c}	Characteristic length	10 μm
k^0	Surface reaction constant	6.0×10^{-8}–6.0×10^{-3} Ω^{-1} cm^{-2}

derived from the EIS measurements because it is often directly correlated to the activity of the material. Two currents can be identified. One is the current linked to the transport of $V_O^{\bullet\bullet}$, which crosses the MIEC|electrolyte interface and travels across the thin film plane. The current due to the transport of e', occurring either in plane or cross-plane depending on the configuration of the current collectors, is confined to the thin film alone. The corresponding resistances are also shown in the schematic circuit of Fig. 2. It is easy to see that R_p, half size of the computed impedance arc, is the sum of the surface reaction resistance R_{surf} and the drift-diffusion resistance R_{DD}:

$$R_p = \frac{1}{2}Z|_{f=0} = R_{surf} + R_{DD} \quad (22)$$

Further, the R_{DD} is given by the sum of the bulk ionic resistance R_{ion} and the electronic resistance R_{eon}

$$R_{DD} = R_{eon} + R_{ion} \quad (23)$$

with

$$R_{eon} = U_T \frac{\langle \delta\hat{\mu}_{eon}{}^* \rangle_{\Gamma_4} - \langle \delta\hat{\mu}_{eon}{}^* \rangle_{\Gamma_5}}{\hat{j}}\bigg|_{f=0} \quad (24a)$$

$$R_{ion} = U_T \frac{\langle \delta\hat{\mu}_{ion}{}^* \rangle_{\Gamma_5} - \langle \delta\hat{\mu}_{eon}{}^* \rangle_{\Gamma_1}}{\hat{j}}\bigg|_{f=0} \quad (24b)$$

As shown in Fig. 3, the numerical results closely follow the experimental data from the Haile group.[32] The model also captures the correct $\tilde{p}_{O_2}$ dependence: the area specific electrode resistance R_p, *i.e.*, the half size of the arc, increases with $\tilde{p}_{O_2}$. In fact, R_p has two contributions according to (23). The first contribution is the surface reaction resistance R_{surf}, which, due to its proportionality with respect to $\tilde{p}_{O_2}^{-\beta}$ ($\beta > 0$), see (16) and (17), increases with $\tilde{p}_{O_2}$. The other contribution is due to the drift-diffusion resistance R_{DD}, which also increases with $\tilde{p}_{O_2}$ because the electrical conductivity σ^0_{eon} decreases when $\tilde{p}_{O_2}$ increases according to (1) and (5).

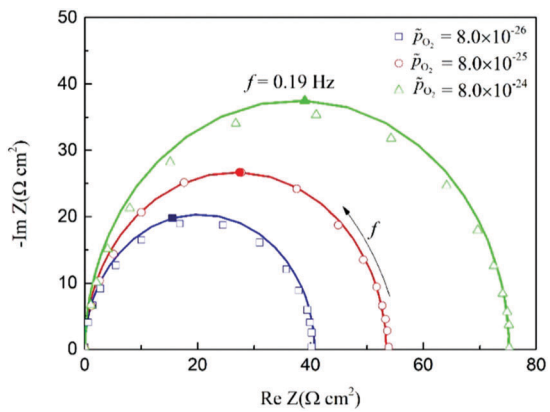

Fig. 3 Computed EIS (solid lines) with $k^0 = 6 \times 10^{-8}$ Ω^{-1} cm^{-2} and l = 195 nm, compared against the experimental data (open symbols) at 650 °C from Chueh and Haile.[32] The filled symbols correspond to f = 0.19 Hz.

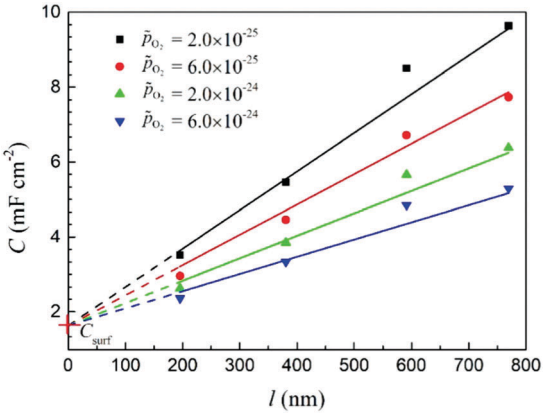

Fig. 4 The film capacitance as a function of film thickness l at 600 °C. Computational results (lines) are compared against experimental data (symbols) at different $\tilde{p}_{O_2}$.

The experimental data can also be compared against a simple RC circuit.[32] Based on such a circuit model, two capacitances can be identified: (i) the capacitance of the bulk, C_{bulk}, defined as the product of C_{chem} and the volume of the sample,[32,35] and (ii) the surface capacitance C_{surf}. While C_{bulk} is a function of the film thickness l, C_{surf} is independent of that quantity. In accordance with the corrected equivalent circuit, the Chang–Jaffé boundary condition (16) can be further generalized, see (18), to include a surface capacitance effect, see ESI,† Section S1. The total capacitance is shown in Fig. 4, where the bulk capacitance increases linearly with l. C_{bulk}, the value of the capacitance at $l = 0$, is estimated to be 1.63 mF cm^{-2}, a value very close to the one we previously computed.[34]

3.1.2 The interplay between 2PB and 3PB density on electrode resistance. As shown by many experiments, the electrochemical activity of SDC is independent of 3PB density.[3,13–16,64,65] Therefore, we tested whether our model can capture the dependence of R_p with respect to the width and spacing of the current collectors. The 2PB and 3PB densities are defined as $d_{2PB} = W_2/(W_1 + W_2)$ and $d_{3PB} = 1/(W_1 + W_2)$, respectively. To study the effect of 2PB density, we fixed $W_1 + W_2$ to 80 μm and varied W_2 from 5 μm to 75 μm. Instead, to investigate the influence of the 3PB density, we set d_{2PB} to 0.5 and varied $W_1 + W_2$ from 5 μm to 80 μm. In Fig. 5, we plot the correspondingly computed $1/R_p$ as a function of 2PB density (panel (a)) and 3PB density (panel (b)). One can easily see that, while $1/R_p$ depends on d_{2PB} with a slope of 1, it is relatively independent of d_{3PB}, showing a slope of 0. Our computational results are again consistent with the experiments.

3.2 Embedded electrode simulation

3.2.1 EIS and electrode resistance in comparison with experiments. For the embedded electrode simulations, we modeled SDC-20, leveraging the experimental data of the Haile group.[3] Further, the patterned Pt strips are placed beneath the electrode and are characterized by a width of 2.5 μm and a 17.5 μm interspacing. This is schematically shown in Fig. 1 panels (b) and (d). We computed the EIS using model (9) (dashed line of Fig. 6) and reported it against experimental

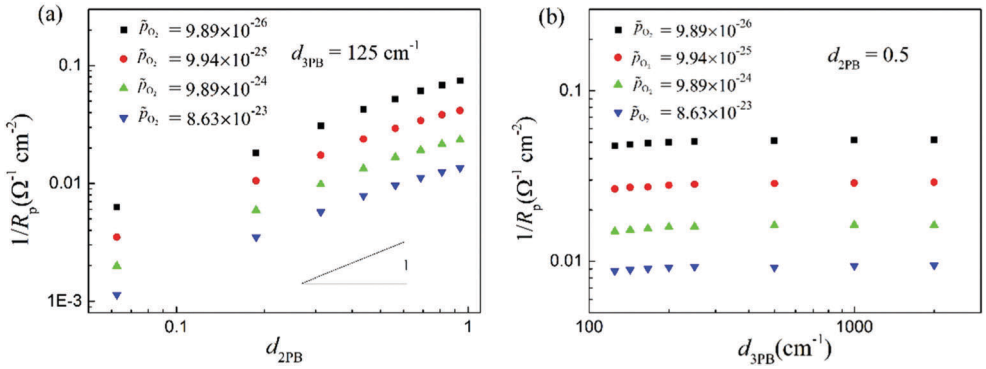

Fig. 5 Inverse electrode polarization as a function of 2PB and 3PB density. The R_p is sensitive to the 2PB density but insensitive to the 3PB density.

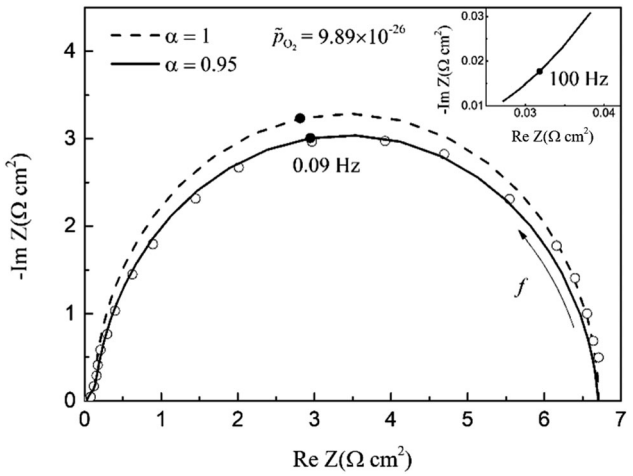

Fig. 6 Numerical EIS (with $k^0 = 5.4 \times 10^{-5}\ \Omega^{-1}\ cm^{-2}$, $\beta = 0.15$, $l = 0.9\ \mu m$, $h = 150$ nm) compared with experimental data. The inset shows the high-frequency part of the Nyquist plot.

data (open circles). It should be noted that the experimental impedance semicircle is slightly depressed. This suggests that the time derivative in (9) should be replaced by a fractional derivative.[66] In other words, the term ∂_t should be substituted by ∂_t^α with a corresponding modification of the Fourier transform, more details are given in the ESI,† Section S3. The fractional derivative model, the solid line in Fig. 6, better matches the EIS.

To further validate our model, we compared the computed R_p against experimental data. As shown in Fig. 7(a), R_p depends on $\tilde{p}_{O_2}$ to the power of 0.15, matching the experiments well.[3] This hints that the electrode resistance R_p is primarily limited by surface reactions, recalling however that R_p has two contributions, see (23): the surface reaction resistance R_{surf} and drift-diffusion resistance R_{DD}. The ratio between the two is defined as the fractional surface resistance, *i.e.*, $f_{surf} = R_{surf}/R_p$. f_{surf} approaches 1 when surface reaction resistance dominates, and 0 when, instead, the two components of the drift-diffusion resistance R_{DD}, see (24), R_{eon} and R_{ion} control R_p.

We varied k^0 to illustrate a transition between surface-reaction-dominated polarization resistance ($f_{surf} \approx 1$) to transport-controlled resistance ($f_{surf} \approx 0$). As shown in Fig. 7(b), when the surface reactions are slow (this corresponds to a small value of k^0), R_p is dominated by the R_{surf} contribution. This leads to $f_{surf} \approx 1$. In contrast, increasing k^0 facilitates the surface reactions and reduces R_{surf} as well as the R_p, increasing the relative contributions from the transport resistances R_{eon} and R_{ion},[41] and the $f_{surf} \approx 0$. This dependence is also in qualitative agreement with our earlier work.[34,40,41]

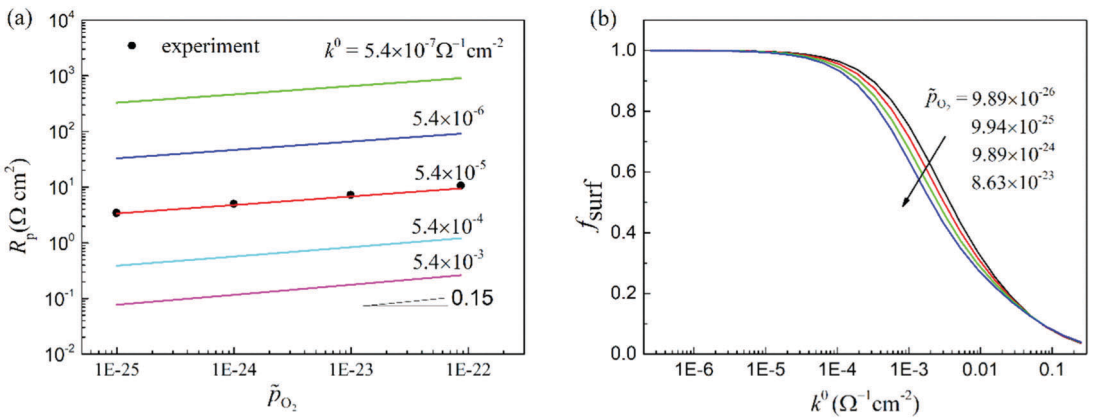

Fig. 7 Total electrode resistance R_p *versus* reaction constant k^0 at various $\tilde{p}_{O_2}$ (a) and fractional surface resistance (b). Experimental data are marked with filled circles.

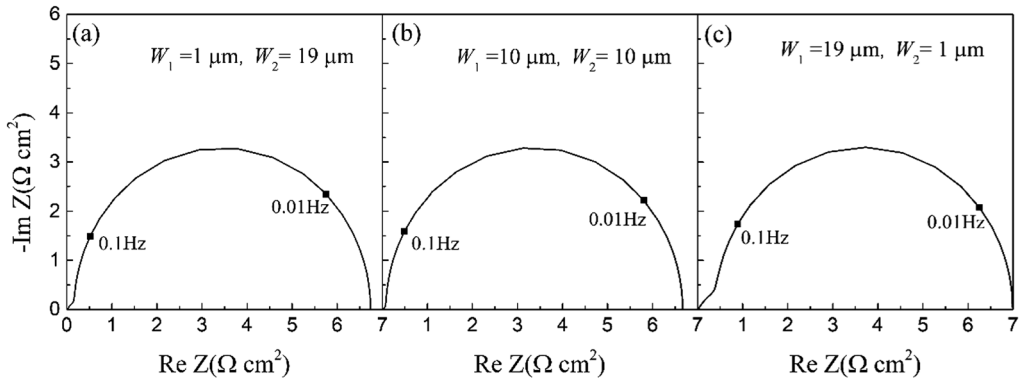

Fig. 8 Computed EIS with variable current collector size, the filled squares indicate select frequencies.

In addition to the placement of current collectors, changing their size will also affect the electrochemical response. To gain an insight into this effect, we set the whole electrode area to be identical to that reported by Chueh and co-workers,[3] *i.e.*, $W_1 + W_2 = 20$ μm, and varied the width W_1 of the current collectors. To focus only on the influence of the geometry, the following simulations were all carried out with $k^0 = 5.4 \times 10^{-5}$ Ω^{-1} cm^{-2} and at $\tilde{p}_{O_2} = 9.89 \times 10^{-26}$ and $T = 650$ °C (this corresponds to $R_{surf} = 3.29$ Ω cm^2). Fig. 8 shows the corresponding EIS responses and indicates that the geometry does have an impact on the Nyquist plot of Z. Not only does the polarization resistance vary with the current collector size but the high-frequency feature emerging from the computations also appears to be highly sensitive to the geometry. It is especially visible when the film is thin (*e.g.* $l \leq 400$ nm) and either $W_1 \gg W_2$ or $W_1 \ll W_2$, see Fig. S2 (ESI†). The high frequency feature significantly affects the R_p when the current collector covers most of the surface ($W_1 \gg W_2$) and the films are thin. In contrast, thicker films (*e.g.* $l = 10$ μm) only display slight deviations from the RC circuit response.

In order to understand the characteristics of this feature, we analyzed in more detail Z in the frequency range from 1 Hz to 15 Hz. We plotted the phase angle θ *versus* frequency (Fig. S3, ESI†), and found that $\theta \approx 45^\circ$ in that range. Further, the real part of Z is proportional to the inverse square root of angular frequency, *i.e.*, Re $Z \propto \omega^{-1/2}$, see Fig. 9. These two results hint at a Warburg-type process. Furthermore, for the configurations of Fig. S4 (ESI†), the slope of Re Z *versus* $\omega^{-1/2}$ decreases with increasing thickness l. Additionally, for thinner films (*e.g.* $l = 200$ nm) with wide metal strips (*e.g.* $W_1 = 19$ μm), the proportionality no longer holds, indicating a much more complicated electrochemical response. This data further suggests that the geometric configuration plays a major role in determining the EIS response. Lastly, we expect that the electrochemical response will be even more complicated if the MIEC|gas or the MIEC|metal interfaces are not flat.[26]

We computed the various resistances schematically shown in Fig. 2(b) to identify their relative role in the R_p. As shown in Fig. 10, an increase of the metal width W_1, decreases R_{eon} and increases R_{ion}, where the two values are very close when $W_1 \approx W_2$. This, of course, is qualitative and only valid for the given thickness.

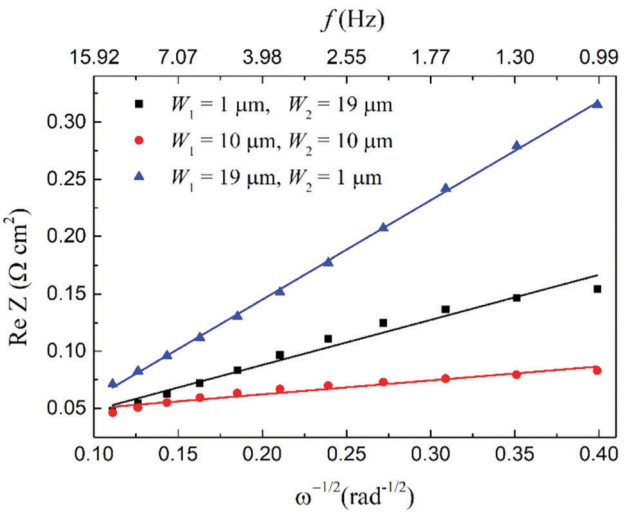

Fig. 9 Re Z *versus* the inverse square root of angular frequency ω for the EIS responses shown in Fig. 8, only the high frequency impedances are shown.

It is important to note that R_p is a quantity, which is typically attributed to surface reactions (*i.e.* it is typically taken that $f_{surf} \approx 1$). However, our results clearly highlight that geometric dimensions of the embedded configuration need to be chosen carefully to minimize the impact of R_{DD} in R_p, see Fig. S3 (ESI†), where a series of Nyquist plots are shown for reference. From a purely empirical point of view, it is interesting to note that the high frequency feature is minimized, see Fig. 8(b), when the two diffusion resistances, R_{eon} or R_{ion}, are identical (Fig. 10).

It may seem counter-intuitive that R_{eon} decreases with W_1 while R_{ion} increases with W_1. However, this dependence can be rationalized by analyzing the flow lines of e' and $V_O^{\bullet\bullet}$ together with their corresponding electrochemical potentials. At $f = 0$, the governing eqn (11) can be decoupled into two Laplace's equations with different boundary conditions (12)–(15), which are connected by the boundary condition (18). In light of the boundary conditions (12)–(15), it is natural to separate the film into two regions:[26] (i) the area above the metal, which is denoted as the current collector (CC) region; (ii) the remaining area above the film substrate, denoted as the ionic

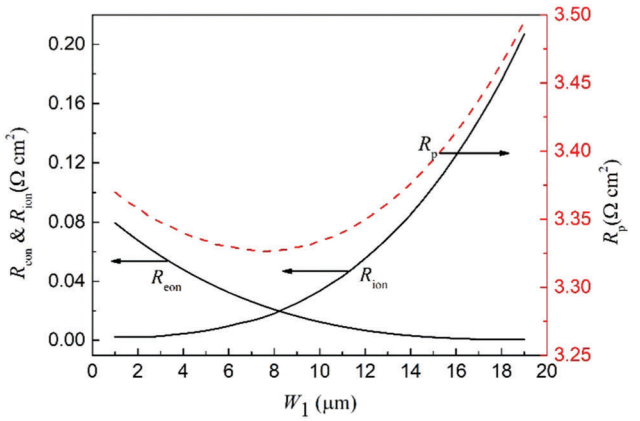

Fig. 10 Total area specific resistance R_p, displayed together with the resistances due to transport R_{eon} and R_{ion} as a function of W_1, the current collector width. The sum of the width and interspacing is fixed, *i.e.*, $W_1 + W_2 = 20$ μm. From the definition (22), R_p is half the size of the impedance arc.

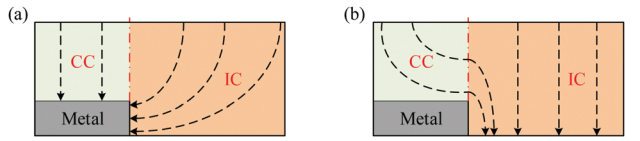

Fig. 11 Schematic illustration of different regions for (a) electrons flow and (b) oxygen vacancies flow in the film.

conductor (IC) region. The separate regions are schematically drawn in Fig. 11. The path of electrons and vacancies occurs preponderantly in one of these regions if the metal current collector is either small or large relative to the spacing. In particular, if $W_1 \ll W_2$, Fig. 12(a), electrons e′ flow vertically in the CC region, and bend horizontally in the IC region. Similarly, if $W_1 \gg W_2$, Fig. 12(f), the oxygen vacancies $V_O^{\bullet\bullet}$ bend horizontally in the CC region, but flow along a straight path into the ionically conductive substrate, in the IC region, instead. Intermediate conditions can be seen in the other panels of Fig. 12. The contour plots of electrochemical potential also confirm the presence of two distinct regions, see Fig. S5 (ESI†), where the gradient of electrochemical potential is distinctively different. Since larger gradients imply larger resistances, we can expect that the major contributions to the transport resistance occur in the regions where $\delta\tilde{\mu}_{eon}$* and/or $\delta\tilde{\mu}_{ion}$* change rapidly. If the interspacing is large relative to the current collector width, the resistance R_{eon} will dominate and be attributed to the IC region. This allows us to write $R_{eon} \sim \frac{1}{\sigma^0_{eon}}\frac{W_2}{l}$. In deriving this approximate relation, we have simply taken that the path of electrons is as long as W_2 and its cross-section is proportional to l and used the definition of the conductivity, *i.e.*, $\sigma = \frac{1}{R}\frac{W}{A}$, where W is the transport length and A is the cross-sectional area. It is important to remark that this analysis is qualitatively in line with the contour plots displayed Fig. S5(a) (ESI†), where the $\delta\tilde{\mu}_{eon}$* is almost constant in the CC region but varies significantly in the IC region. In a similar manner, we can estimate R_{ion} when W_2 is sufficiently large. Using an identical argument, we can write $R_{ion} \sim \frac{1}{\sigma^0_{ion}}\frac{W_1}{l-h}$. Again, the analysis agrees with the 2D plots of $\delta\tilde{\mu}_{ion}$*, see Fig. S5(d) (ESI†), where the preponderant drop of reduced electrochemical potential occurs in the CC region.

We also explored the influence of the film thickness and the width and interspacing of the current collectors on the area specific resistance R_p. Since we set R_{surf} to be constant, R_p is only sensitive to R_{eon} and R_{ion} according to (22) and (23), where $R_p = R_{surf} + R_{eon} + R_{ion}$. We first plotted the R_{eon} and R_{ion} as a function of the thickness and current collector size in Fig. 13(a) and (b), respectively. Both resistances decrease with the film thickness for extremal values of W_1 and W_2, that is when the current collector is either narrow or wide. This is contrary to the impression obtained from Fig. 2 that shortening the transport distance lowers the resistance, and can be understood using the schematic in Fig. 11.

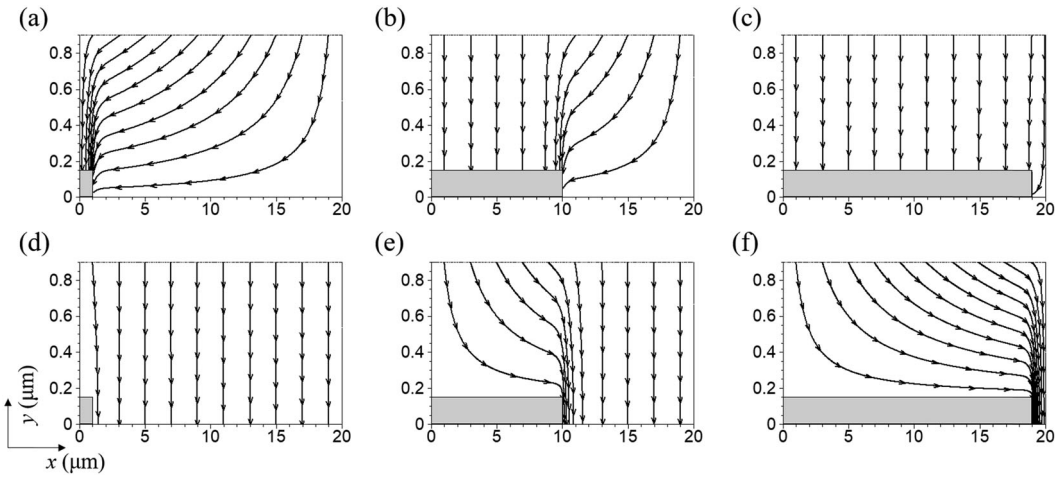

Fig. 12 Flow lines of (a)–(c) electrons and (d)–(f) oxygen vacancies for different widths of current collector with $f = 0$, (a) and (d) $W_1 = 1$ μm, $W_2 = 19$ μm, (b) and (e) $W_1 = 10$ μm, $W_2 = 10$ μm, (c) and (f) $W_1 = 19$ μm, $W_2 = 1$ μm.

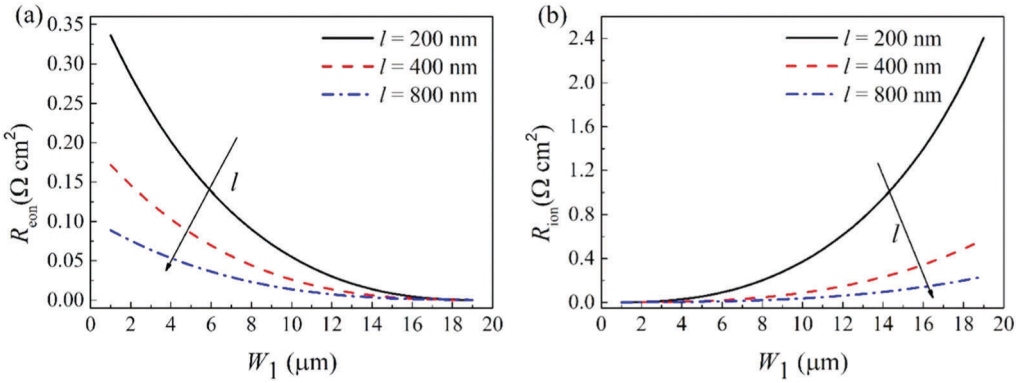

Fig. 13 The electronic resistance R_{eon} and the ionic resistance R_{ion} for 150 nm-high current collectors with variable width W_1 (with $W_1 + W_2$ = 20 μm) and variable thickness l.

To further illustrate this mechanism, the flow lines with specific geometric parameters (W_1 = 1 μm, W_2 = 19 μm for electrons, W_1 = 19 μm, W_2 = 1 μm for ions) are shown in Fig. 14, and the corresponding reduced electrochemical potentials are shown in Fig. S6 (ESI†). In fact, it is expected that increasing the thickness results in more uniform currents and the electrochemical potential variations across the 2PB. For electrons transport with a narrow current collector, *i.e.*, W_1 = 1 μm, $\delta\hat{\mu}_{eon}$* varies significantly in the IC region and is constant in the CC region, see Fig. S6(a) and (c) (ESI†). The main contribution of R_{eon} can be attributed to the specific transport resistance in the IC region where $\delta\hat{\mu}_{eon}$* varies with greatest gradient. Consequently, we can write $R_{eon} \sim \frac{1}{\sigma^0_{eon}}\frac{W_2}{l}$ and the corresponding

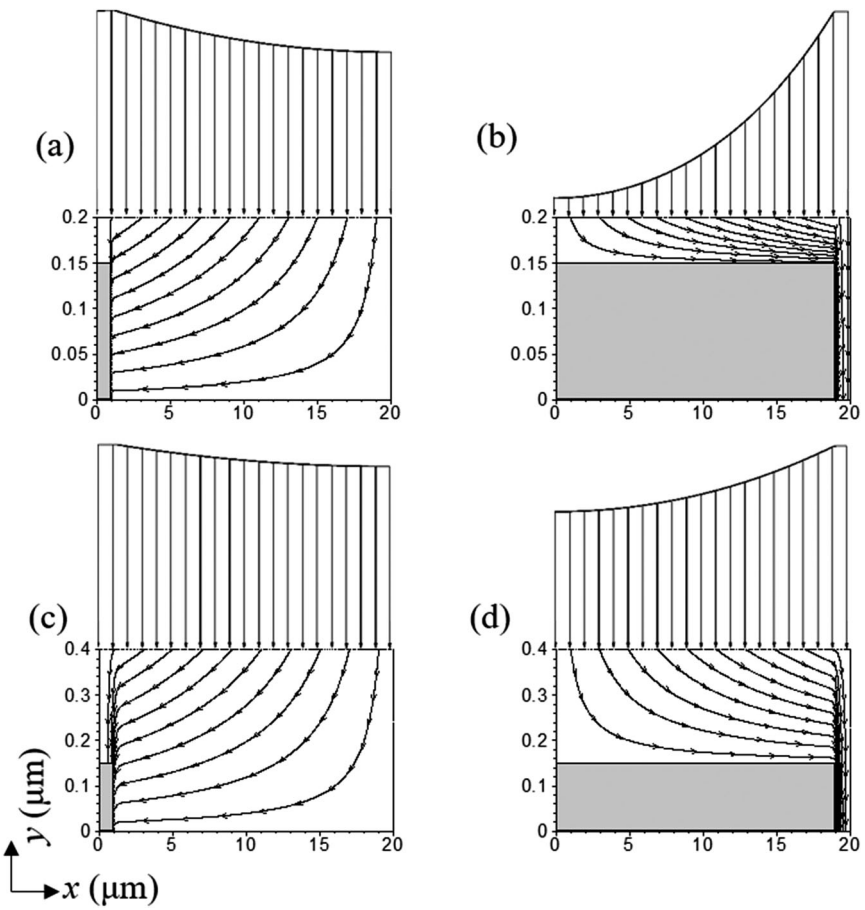

Fig. 14 Flow lines of electrons, (a) and (c), and oxygen vacancies, (b) and (d) for different geometry parameters at 0 frequency, (a) and (c) with W_1 = 1 μm, W_2 = 19 μm, (b) and (d) with W_1 = 10 μm, W_2 = 10 μm, the film thickness is 200 nm in (a) and (b), 400 nm in (c) and (d). The current density at the top surface and normalized with respect to its maximum value is also shown.

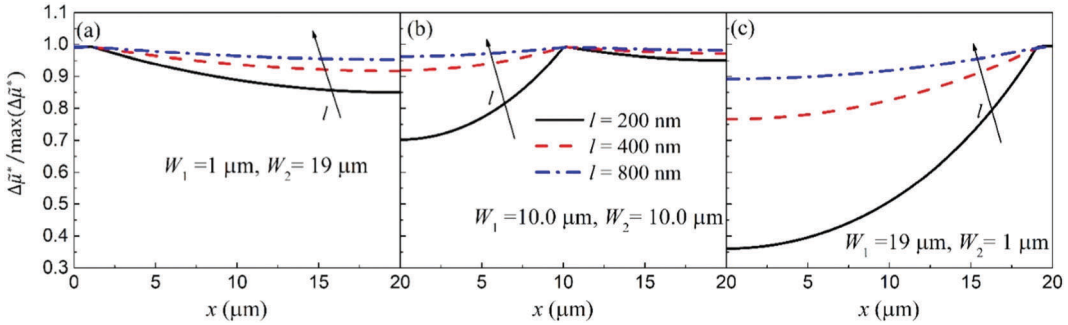

Fig. 15 Distribution of normalized electrochemical potential change along the reaction interface with varied geometry parameters.

flow lines are shown in Fig. 14(a) and (c). On the other hand, for a wide current collector, *i.e.*, $W_1 = 19$ μm, $\delta\hat{\mu}_{ion}^*$ varies mainly in the CC region, and remains unchanged in the IC region, see Fig. S6(b) and (d) (ESI†). Similarly, one can expect that R_{ion} is mainly due to the transport resistance in the CC region, and we can estimate $R_{ion} \sim \frac{1}{\sigma_{ion}^0}\frac{W_1}{l-h}$. This is also demonstrated with flow lines shown in Fig. 14(b) and (d), where $V_O^{\bullet\bullet}$ bend horizontally in the CC region, and flow vertically to penetrate the MIEC|electrolyte interface. Therefore, with the above analysis of R_{eon} and R_{ion}, it is easy to conclude that both the electronic diffusion resistance R_{eon} and the ionic resistance R_{ion} drop when the film thickness increases. And their contributions are minimized when the film thickness is high.

We also investigated the actual activity of the 2PB with embedded current collectors. The activity is correlated to the local electronic current density normal to the surface $\boldsymbol{j}_{eon}\cdot\mathbf{n}$, which is, in turn, proportional to the electrochemical potential difference that drives the electrochemical reactions, *i.e.*, $\Delta\tilde{\mu}^* = \delta\tilde{\mu}_{eon}^* - \delta\tilde{\mu}_{ion}^*$. This is obtained from the Chang–Jaffé boundary condition, see (18).[41] Fig. 15 shows the distribution of $\Delta\tilde{\mu}^*$ along the MIEC|gas surface, normalized by its maximum value $\max(\Delta\tilde{\mu}^*)$. With an increase of film thickness, $\Delta\tilde{\mu}^*$ is on average larger and more uniformly distributed. With a fixed electrochemical potential drop across the film, see (20), a larger value of the current implies a smaller R_p. This is also in agreement with the analysis of the specific resistances linked to Fig. 13.

Furthermore, one can notice that the $\Delta\tilde{\mu}^*$ has an inflection at the 2PB, where such inflection mimics the presence current collector. This feature can be primarily seen for small film thicknesses, effectively mirroring the boundary conditions at the bottom of the computational domain. In contrast, the distribution along the surface is nearly flat if the film thickness is sufficiently high. As shown in Fig. 13, both the electronic and ionic transport resistances decrease with l, further supporting the dominant role of surface reactions if the film is sufficiently thick. Additionally, the distribution of $\Delta\tilde{\mu}^*$ just represents the current flux in the film. For a narrow current collector, *i.e.* $W_1 = 1$ μm, most of the electrons and oxygen vacancies transport in the IC region. However, increasing the width of current collector results in the redistribution of $\Delta\tilde{\mu}^*$, as well as the current flux. When W_1 is much larger, *e.g.* $W_1 = 19$ μm, most of the mobile species transport in the CC region. This is also shown in the flow lines in Fig. 13 and 14.

4 Conclusions

In this article, we have developed a novel numerical framework for the study of the EIS of thin film MIECs. Our model, which features the transport of two defects and their reaction at the surface where the MIEC is exposed to the external gas, was validated against SDC experimental data for configurations where the current collector is either exposed to the gas or embedded into the MIEC. We were able to fit the experimental EIS response by adjusting only the surface reaction rate. We also computed the capacitance and the polarization (*vs.* $\tilde{p}_{O_2}$) of the films with values near those experimentally measured.

In the embedded configuration, which is widely believed to minimize the impact of the current collectors, we interestingly found that the current collector width and spacing can have a significant influence on the EIS response. We saw this impact in two ways. First, a new feature appears in the impedance at sufficiently high frequencies, suggesting a complex interplay between ionic and electronic transport. Second, the area specific resistance, a quantity typically attributed to the surface reactions only, is sensitive to the film thickness and the current collector configuration. This effect results in an increased polarization resistance. This is particularly true for thinner films, which generally result in increased transportation losses. This contribution increases with the width of the current collectors. Interestingly, our model also shows that for thinner films the surface reactivity is far from uniform and displays features directly mirroring the placement of the current collector.

Conflicts of interest

There are no conflicts to declare.

Notes and references

1 S. Chu and A. Majumdar, *Nature*, 2012, **488**, 294–303.
2 S. C. Singhal and K. Kendall, *High-temperature solid oxide fuel cells: fundamentals, design and applications*, Elsevier, 2003.
3 W. C. Chueh, Y. Hao, W. Jung and S. M. Haile, *Nat. Mater.*, 2011, **11**, 155–161.
4 W. Jung, J. O. Dereux, W. C. Chueh, Y. Hao and S. M. Haile, *Energy Environ. Sci.*, 2012, **5**, 8682–8689.

5 A. B. Stambouli and E. Traversa, *Renewable Sustainable Energy Rev.*, 2002, **6**, 433–455.
6 W. G. Bessler, M. Vogler, H. Stormer, D. Gerthsen, A. Utz, A. Weber and E. Ivers-Tiffee, *Phys. Chem. Chem. Phys.*, 2010, **12**, 13888–13903.
7 S. B. Adler, J. Lane and B. Steele, *J. Electrochem. Soc.*, 1996, **143**, 3554–3564.
8 K. Yashiro, T. Nakamura, M. Sase, F. Hermes, K. Sato, T. Kawada and J. Mizusaki, *Electrochem. Solid-State Lett.*, 2009, **12**, B135–B137.
9 J. Suntivich, K. J. May, H. A. Gasteiger, J. B. Goodenough and Y. Shao-Horn, *Science*, 2011, **334**, 1383–1385.
10 L. dos Santos-Gómez, E. Losilla, F. Martín, J. Ramos-Barrado and D. Marrero-López, *ACS Appl. Mater. Interfaces*, 2015, **7**, 7197–7205.
11 D. Chen, C. Chen, F. Dong, Z. Shao and F. Ciucci, *J. Power Sources*, 2014, **250**, 188–195.
12 W. C. Chueh, W. Lai and S. M. Haile, *Solid State Ionics*, 2008, **179**, 1036–1041.
13 C. Zhang, M. E. Grass, A. H. McDaniel, S. C. DeCaluwe, F. El Gabaly, Z. Liu, K. F. McCarty, R. L. Farrow, M. A. Linne, Z. Hussain, G. S. Jackson, H. Bluhm and B. W. Eichhorn, *Nat. Mater.*, 2010, **9**, 944–949.
14 Y. Choi, E. C. Brown, S. M. Haile and W. Jung, *Nano Energy*, 2016, **23**, 161–171.
15 Z. A. Feng, F. El Gabaly, X. Ye, Z. X. Shen and W. C. Chueh, *Nat. Commun.*, 2014, **5**, 4374, DOI: 10.1038/ncomms5374.
16 S. Park, J. M. Vohs and R. J. Gorte, *Nature*, 2000, **404**, 265–267.
17 N. Yang, A. Belianinov, E. Strelcov, A. Tebano, V. Foglietti, D. Di Castro, C. Schlueter, T.-L. Lee, A. P. Baddorf and N. Balke, *ACS Nano*, 2014, **8**, 12494–12501.
18 S. Zha, W. Rauch and M. Liu, *Solid State Ionics*, 2004, **166**, 241–250.
19 A. Kulkarni, F. T. Ciacchi, S. Giddey, C. Munnings, S. P. S. Badwal, J. A. Kimpton and D. Fini, *Int. J. Hydrogen Energy*, 2012, **37**, 19092–19102.
20 D. Neagu, G. Tsekouras, D. N. Miller, H. Menard and J. T. Irvine, *Nat. Chem.*, 2013, **5**, 916–923.
21 J. H. Myung, D. Neagu, D. N. Miller and J. T. Irvine, *Nature*, 2016, **537**, 528–531.
22 H. He, J. M. Vohs and R. J. Gorte, *J. Electrochem. Soc.*, 2003, **150**, A1470–A1475.
23 H. He, *Solid State Ionics*, 2004, **175**, 171–176.
24 S. McIntosh, J. M. Vohs and R. J. Gorte, *J. Electrochem. Soc.*, 2003, **150**, A470–A476.
25 S. McIntosh, J. M. Vohs and R. J. Gorte, *J. Electrochem. Soc.*, 2003, **150**, A1305–A1312.
26 A. Nenning, A. K. Opitz, T. M. Huber and J. Fleig, *Phys. Chem. Chem. Phys.*, 2014, **16**, 22321–22336.
27 J. Fleig, F. S. Baumann, V. Brichzin, H. R. Kim, J. Jamnik, G. Cristiani, H. U. Habermeier and J. Maier, *Fuel Cells*, 2006, **6**, 284–292.
28 F. S. Baumann, J. Maier and J. Fleig, *Solid State Ionics*, 2008, **179**, 1198–1204.
29 C. Graves, L. Martinez and B. R. Sudireddy, *ECS Trans.*, 2016, **72**, 183–192.
30 W. H. Kan, A. J. Samson and V. Thangadurai, *J. Mater. Chem. A*, 2016, **4**, 17913–17932.
31 R. Sinclair, S. C. Lee, Y. Shi and W. C. Chueh, *Ultramicroscopy*, 2017, **175**, 25–35.
32 W. C. Chueh and S. M. Haile, *Phys. Chem. Chem. Phys.*, 2009, **11**, 8144–8148.
33 J. Mizusaki, H. Tagawa, T. Saito, T. Yamamura, K. Kamitani, K. Hirano, S. Ehara, T. Takagi, T. Hikita and M. Ippommatsu, *Solid State Ionics*, 1994, **70**, 52–58.
34 C. Chen, D. Chen, W. C. Chueh and F. Ciucci, *Phys. Chem. Chem. Phys.*, 2014, **16**, 11573–11583.
35 S. Kogler, A. Nenning, G. M. Rupp, A. K. Opitz and J. Fleig, *J. Electrochem. Soc.*, 2015, **162**, F317–F326.
36 W. C. Chueh, A. H. McDaniel, M. E. Grass, Y. Hao, N. Jabeen, Z. Liu, S. M. Haile, K. F. McCarty, H. Bluhm and F. El Gabaly, *Chem. Mater.*, 2012, **24**, 1876–1882.
37 M. E. Orazem and B. Tribollet, *Electrochemical impedance spectroscopy*, John Wiley & Sons, 2011.
38 E. Barsoukov and J. R. Macdonald, *Impedance spectroscopy: theory, experiment, and applications*, John Wiley & Sons, 2005.
39 J. Fleig, *J. Electroceram.*, 2004, **13**, 637–644.
40 F. Ciucci, Y. Hao and D. G. Goodwin, *Phys. Chem. Chem. Phys.*, 2009, **11**, 11243–11257.
41 F. Ciucci, W. C. Chueh, D. G. Goodwin and S. M. Haile, *Phys. Chem. Chem. Phys.*, 2011, **13**, 2121–2135.
42 K. Miyawaki, M. Kishimoto, H. Iwai, M. Saito and H. Yoshida, *J. Power Sources*, 2014, **267**, 503–514.
43 M. Kishimoto, H. Iwai, K. Miyawaki, M. Saito and H. Yoshida, *J. Power Sources*, 2013, **223**, 268–276.
44 M. Kishimoto, H. Iwai, M. Saito and H. Yoshida, *J. Electrochem. Soc.*, 2012, **159**, B315–B323.
45 T. Carraro, J. Joos, B. Rüger, A. Weber and E. Ivers-Tiffée, *Electrochim. Acta*, 2012, **77**, 309–314.
46 T. Carraro, J. Joos, B. Rüger, A. Weber and E. Ivers-Tiffée, *Electrochim. Acta*, 2012, **77**, 315–323.
47 A. Haffelin, J. Joos, M. Ender, A. Weber and E. Ivers-Tiffee, *J. Electrochem. Soc.*, 2013, **160**, F867–F876.
48 J. Joos, M. Ender, T. Carraro, A. Weber and E. Ivers-Tiffée, *Electrochim. Acta*, 2012, **82**, 268–276.
49 M. Kishimoto, M. Lomberg, E. Ruiz-Trejo and N. P. Brandon, *Electrochim. Acta*, 2016, **190**, 178–185.
50 J. Jamnik and J. Maier, *Phys. Chem. Chem. Phys.*, 2001, **3**, 1668–1678.
51 H. Zhu, A. Kromp, A. Leonide, E. Ivers-Tiffee, O. Deutschmann and R. J. Kee, *J. Electrochem. Soc.*, 2012, **159**, F255–F266.
52 R. Armstrong, R. Firman and H. Thirsk, *Faraday Discuss. Chem. Soc.*, 1973, **56**, 244–263.
53 I. Epelboin, C. Gabrielli, M. Keddam and H. Takenouti, *Electrochemical Materials Science*, Springer, 1981, pp. 151–192.
54 D. D. Macdonald, *Electrochim. Acta*, 2006, **51**, 1376–1388.
55 A. Atkinson, S. Barnett, R. J. Gorte, J. Irvine, A. J. McEvoy, M. Mogensen, S. C. Singhal and J. Vohs, *Nat. Mater.*, 2004, **3**, 17–27.
56 F. Kröger and H. Vink, *Solid State Phys.*, 1956, **3**, 307–435.
57 W. Lai and S. M. Haile, *J. Am. Ceram. Soc.*, 2005, **88**, 2979–2997.

58 S. M. Sze and K. K. Ng, *Physics of semiconductor devices*, John wiley & Sons, 2006.
59 W. Lai, PhD thesis, California Institute of Technology, 2007.
60 W. Lai and S. M. Haile, *Phys. Chem. Chem. Phys.*, 2008, **10**, 865–883.
61 H. C. Chang and G. Jaffé, *J. Chem. Phys.*, 1952, **20**, 1071–1077.
62 F. Hecht, *J. Numer. Math.*, 2012, **20**, 251–266.
63 S. Brenner and R. Scott, *The mathematical theory of finite element methods*, Springer Science & Business Media, 2007.
64 T. Nakamura, T. Kobayashi, K. Yashiro, A. Kaimai, T. Otake, K. Sato, J. Mizusaki and T. Kawada, *J. Electrochem. Soc.*, 2008, **155**, B563–B569.
65 W. Jung and H. L. Tuller, *Adv. Energy Mater.*, 2011, **1**, 1184–1191.
66 I. Podlubny, *Fractional differential equations: an introduction to fractional derivatives, fractional differential equations, to methods of their solution and some of their applications*, Academic Press, 1998.